

Screening A-site ordered quadruple perovskites for alkaline hydrogen evolution reaction via unifying electronic configuration descriptor

Ning Sun(孙宁), Wenbo Li(李文博), Yang Qin(秦杨), Zhichuan Zheng(郑智钏), Bowen Zhang(张博文), Xiangjiang Dong(董祥江), Peng Wei(魏鹏), Yixiao Zhang(张艺潇), Xian He(何贤), Xinyu Xie(谢新煜), Kai Huang(黄凯), Lailei Wu(吴来磊), Ming Lei(雷鸣), Huiyang Gou(缑慧阳), and Runze Yu(于润泽)
Citation: Chin. Phys. B, 2024, 33 (**12**): 128101. DOI: 10.1088/1674-1056/ad8074
Journal homepage: http://cpb.iphy.ac.cn; http://iopscience.iop.org/cpb

What follows is a list of articles you may be interested in

Regulating the dopant clustering in LiZnAs-based diluted magnetic semiconductor

Zihang Jia(贾子航), Bo Zhou(周波), Zhenyi Jiang(姜振益), and Xiaodong Zhang(张小东)
Chin. Phys. B, 2024, 33 (**5**): 058101. DOI: 10.1088/1674-1056/ad3034

Epitaxial growth of ultrathin gallium films on Cd(0001)

Zuo Li(李佐), Mingxia Shi(石明霞), Gang Yao(姚钢), Minlong Tao(陶敏龙), and Junzhong Wang(王俊忠)
Chin. Phys. B, 2024, 33 (**1**): 018101. DOI: 10.1088/1674-1056/acfb7a

Molecular dynamics study of thermal conductivities of cubic diamond, lonsdaleite, and nanotwinned diamond via machine-learned potential

Jia-Hao Xiong(熊佳豪), Zi-Jun Qi(戚梓俊), Kang Liang(梁康), Xiang Sun(孙祥), Zhan-Peng Sun(孙展鹏), Qi-Jun Wang(汪启军), Li-Wei Chen(陈黎玮), Gai Wu(吴改), and Wei Shen(沈威)
Chin. Phys. B, 2023, 32 (**12**): 128101. DOI: 10.1088/1674-1056/ace4b4

Enhanced xylene sensing performance of hierarchical flower-like Co_3O_4 via In doping

Jing Zhang(张京), Jianyu Ling(凌剑宇), Kuikun Gu(谷魁坤), Georgiy G. Levchenko, and Xiao Liang(梁霄)
Chin. Phys. B, 2023, 32 (**6**): 068104. DOI: 10.1088/1674-1056/acbe30

Suppression and compensation effect of oxygen on the behavior of heavily boron-doped diamond films

Li-Cai Hao(郝礼才), Zi-Ang Chen(陈子昂), Dong-Yang Liu(刘东阳), Wei-Kang Zhao(赵伟康),Ming Zhang(张鸣), Kun Tang(汤琨), Shun-Ming Zhu(朱顺明), Jian-Dong Ye(叶建东),Rong Zhang(张荣), You-Dou Zheng(郑有炓), and Shu-Lin Gu(顾书林)
Chin. Phys. B, 2023, 32 (**3**): 038101. DOI: 10.1088/1674-1056/ac7f8a

---

Screening *A*-site ordered quadruple perovskites for alkaline hydrogen evolution reaction via unifying electronic configuration descriptor

Ning Sun(孙宁)[1], Wenbo Li(李文博)[2,4], Yang Qin(秦杨)[1], Zhichuan Zheng(郑智钏)[1], Bowen Zhang(张博文)[2], Xiangjiang Dong(董祥江)[2], Peng Wei(魏鹏)[2], Yixiao Zhang(张艺潇)[1], Xian He(何贤)[1], Xinyu Xie(谢新煜)[1], Kai Huang(黄凯)[1,†], Lailei Wu(吴来磊)[3,4,‡], Ming Lei(雷鸣)[1], Huiyang Gou(缑慧阳)[2], and Runze Yu(于润泽)[2,§]

[1] *State Key Laboratory of Information Photonics and Optical Communications, School of Science, Beijing University of Posts and Telecommunications (BUPT), Beijing* 100876, *China*
[2] *Center for High Pressure Science and Technology Advanced Research, Beijing* 100193, *China*
[3] *College of Material Science and Engineering, Liaoning Technical University, Fuxin* 123000, *China*
[4] *College of Material Science and Engineering, Yanshan University, Qinhuangdao* 066004, *China*

(Received 3 September 2024; revised manuscript received 25 September 2024; accepted manuscript online 27 September 2024)

Dynamic adsorption processes of reaction intermediates for alkaline hydrogen evolution (HER) catalysts are still confusing to understand. Here, we report a series of *A*-site ordered quadruple perovskite ruthenium-based electrocatalysts $ACu_3Ru_4O_{12}$ (A = Na, Ca, Nd, and La), with the target sample $SrCu_3Ru_4O_{12}$ exhibiting a very low overpotential (46 mV @10 mA· cm^{-2}) and excellent catalytic stability with little decays after 48-h durability test. Precise tuning *A*-site cations can change the average valence state of Cu and Ru, thus the plot of HER activity *versus* the average Ru valence number shows a volcano-type relationship. Density functional theory indicates that the Ru 4d orbitals of $SrCu_3Ru_4O_{12}$ possesses the most suitable d-band center position among the five samples, which might be the key parameter to determine the catalytic performance. Our work provides further insight into the discovering advanced, efficient hydrogen evolution catalysts through designing precise descriptor.

Keywords: Ru-based electrocatalyst, density functional theory, descriptor, quadruple perovskites, hydrogen evolution reaction

PACS: 81.05.Zx, 81.16.Hc, 88.30.em, 82.20.–w **DOI:** 10.1088/1674-1056/ad8074

1. Introduction

Globally, hydrogen energy constitutes a fundamental element in achieving net-zero emissions and developing a future sustainable growth strategy.[1–3] To product low-cost green hydrogen, water electrolysis offers a pivotal role in the advancement of sustainable energy systems. The alkaline hydrogen evolution reaction (HER) serves to mitigate corrosion and dissolution challenges in acidic media, with pure hydrogen generation exceeding 99.7%.[4,5] This process presents enhanced prospects for industrial-scale applications. Presently, platinum (Pt)-based materials has been extensively investigated as the benchmark and capable electrocatalyst for HER; however, the scarcity and high cost restrict its large-scale commercial applications.[6,7] Additionally, the intrinsic activity of Pt for alkaline HER is 1–2 orders of magnitude less effective than that in the acidic medium owing to insufficient protons for H_2 production.[8,9] Conversely, ruthenium (Ru), with a hydrogen bonding strength ($\sim$ 65 kcal·mol^{-1}) comparable with Pt, is proposed as a promising HER catalyst.[10–12] Moreover, Ru offers a cost-effective alternative to Pt and demonstrates superior efficiency in facilitating water dissociation, and exhibits exceptional performance in chemisorption of intermediate hydroxyl groups.[13,14] Hence, the development of effective Ru-based electrocatalysts is imperative to accelerate HER process and ensure the commercial viability of future electrochemical conversion technologies for large-scale hydrogen production.

Precise design over the adsorption capacity of Ru-based electrocatalysts, including the dynamic adjustment of interactions with intermediates, is vital for targeting electrochemical reactions.[15] Thus, it is crucial to identify suitable single-phase compound platforms that can incorporate multiple elements while maintaining robust crystal stability.[16,17] This ensures effective optimization of surface electronic properties and minimizes interference from dynamic surface reconstruction. Extensive efforts, including crystal and electronic structure modification, are being employed for the strategic design and precise fabrication of Ru-based single-phase catalysts. Perovskites are interesting materials with intriguing properties for exploring diverse ground-state properties and green chemistry applications. In the pure-phase perovskite oxide family (unit perovskites ABO_3, layered perovskites A_2BO_4, double perovskites $A_2BB'O_6$, triple perovskites $A_2A'B_2B'O_9$, and quadruple perovskites $AA'_3B_4O_{12}$), the notable compositional diversity offers substantial advantages for the precise tun-

†Corresponding author. E-mail: huang-kai@bupt.edu.cn
‡Corresponding author. E-mail: wulailei@lntu.edu.cn
§Corresponding author. E-mail: runze.yu@hpstar.ac.cn

© 2024 Chinese Physical Society and IOP Publishing Ltd

ing of Ru-based electronic configurations.[18–21] For instance, the layered Ruddlesden–Popper (RP)-type Sr_2RuO_4 demonstrates exceptional HER electrocatalytic activity (61 mV at 10 mA·cm^{-2}), attributed to the synergistic effect of efficient water dissociation in the SrO layer and favorable hydrogen adsorption and evolution at the apical oxygen sites.[22] Dai *et al*. have developed an efficient HER electrocatalyst $SrTi_{0.7}Ru_{0.3}O_{3-\delta}$ via super-exchange to realize atomic-scale synergistic active centers between Ti, Ru, and O sites.[23] However, conventional ruthenium-based perovskite catalysts frequently undergo surface reconstruction, including Ru amorphization and element aggregation, under high potentials and repeated cycling, which obstructs the development of highly stable catalysts. The *A*-site ordered quadruple perovskite oxide $AA'_3Ru_4O_{12}$ offers a novel strategy for achieving highly active and stable catalytic performance, achieved by incorporating multiple transition metals and tunable Ru–O_6 octahedra through the careful selection of *A*-site elements.[24–26] Due to the strong covalent bonding of each oxygen atom with A' and *B* ions, the overlap between the 3d and O 2p orbitals enables charge transfer through orbital hybridization and local optimization mechanisms.[27] Recently, the role of *A*-sites has been increasingly recognized, as they can serve as important descriptors that significantly influence structural and thermodynamic factors to regulate active sites.[28,29] However, precise *A*-site controlling in quadruple perovskites to enhance the charge adsorption capability of Ru active sites for intermediates, and thereby achieve higher alkaline HER activity, remains an area that needs further investigation.

Descriptors are essential in the design of electrocatalysts, as they offer invaluable insights for the meticulous development of catalysts and minimize costs associated with trial-and-error approaches. In recent decades, there has been a growing emphasis on the exploration of more universal descriptors through electronic and structural characterization.[30,31] This approach holds the potential to foster the establishment of structure–efficacy relationships, thereby informing the prediction of advanced catalysts. Recently, primary descriptors, including the d-band center and spin-related intrinsic property descriptors, have been investigated to enhance the understanding of electrocatalytic processes.[32] Notably, the d-band center mechanism, regarded as a crucial tool, establishes a connection between the absorption and desorption of reaction intermediates and intrinsic activity.[33] Nonetheless, integrating multiple descriptors and identifying the most valuable ones continue to pose significant challenges.

In this paper, we report a quadruple perovskite oxide $SrCu_3Ru_4O_{12}$ as a highly catalyst for HER in alkaline solution. Remarkably, this complex perovskite oxide demonstrates an outstanding overpotential of 46 mV at 10 mA·cm^{-2} and a low Tafel slope of 56 mV·dec^{-1}. This level of catalytic performance is competitive among the reported for Ru-based unmodified pure-phase perovskite oxides and comparable to the most active noble metal catalyst Pt/C. Additionally, our $SrCu_3Ru_4O_{12}$ electrocatalyst demonstrates robust stability, maintaining performance up to 48 hours at 10 mA·cm^{-2} and withstanding 10^4 cycles without performance degradation. To investigate the influence of *A*-site elements on active sites, a series of $ACu_3Ru_4O_{12}$ (A = Na, Ca, Nd, and La) are fabricated to investigate the electronic configuration catalyst descriptor. Density functional theory (DFT) analysis and corresponding characterization confirm that different *A*-site elements affect the shift of the Ru d-band center and O p-band center towards the Fermi level. Orbital hybridization further refines the electronic configuration, allowing for precise adjustment of the adsorption strength at Ru sites, which enhances catalytic activity and improves HER performance. The stable platform and associated multi-integratable parameters present a valuable opportunity to explore descriptor issues in greater depth. Our work will provide valuable insight into the *A*-site element's role in tuning the electronic configuration of quadruple perovskites, and will affect a wide range of descriptor design and energy applications.

2. Experimental details

2.1. Preparation of $ACu_3Ru_4O_{12}$

All samples with different structural entropies were prepared by a modified solid-state method. Firstly, the high-purity individual elements were weighed according to the nominal ratio, and then ground to be mixed uniformly. After pressing them into sheets, they are sintered in a muffle furnace using 950 °C for 48 h ($NaCu_3Ru_4O_{12}$) and 1050 °C for 48 h (other samples). It is important to note that after the sintering process, all samples will undergo further grinding and pressing to form sheets, which will then undergo additional sintering for several cycles to make the phase as pure as possible.

2.2. Material characterizations

Morphology of the samples was observed on field-scanning transmission electron microscopy (TEM) images acquired on a JEM-ARM200F transmission electron microscope operated at 200 kV and scanning transmission electron microscopy (FE-SEM, S-4800, Japan) equipped with energy dispersion spectra (EDS) and elemental mapping. Powder XRD patterns were acquired at room temperature, using an x-ray diffractometer (D/max 2500 V) attached with Cu $K\alpha$ radiation at an operating voltage and current of about 40 kV and 150 mA, respectively. Rietveld refinements for XRD were conducted to obtain detailed structural and compositional information using GSAS (II) software. The element contents in the catalysts were determined by inductively coupled plasma optical emission spectrometer (ICP-OES) on a Agilent 5110. XPS measurements were obtained using an x-ray photoelectron spectrometer (Escalab 250Xi) equipped with an Al $K\alpha$ radiation source (1487.6 eV) and a hemispherical analyzer with a pass energy of 30.0 eV and an energy step size of 0.05 eV.

The binding energy of the C 1s peak at 284.8 eV was considered as an internal reference.

2.3. Material characterizations

For the preparation of catalyst ink, all catalyst powders were dispersed into a mixture solution (200 μl of ethanol, 800 μl of ultrapure water), respectively. The catalyst was ultrasonically dispersed in ink. The obtained catalyst inks were uniformly loaded onto freshly carbon paper electrodes (0.5 mm×0.5 mm) to form the work electrode. The amount of deposited catalyst was calculated to be ∼ 250 μg and the loading on the working electrode was controlled to be 1 mg·cm^{-2}. The HER performance of these samples was characterized in a CHI 760 potentiostat with a three-electrode system in 1.0 M KOH. All polarization curves were collected at a scan rate of 5 mV·s^{-1} and calibrated to the reversible hydrogen electrode according to the following equation: $E_{\mathrm{RHE}} = E_{\mathrm{Hg/HgO}} + 0.098 + 0.059 \times \mathrm{pH}$. An IR compensation level of 90% based on the electrochemical impedance spectroscopy. ECSA analysis was used CVs taken at various scan rates (10 mV·s^{-1}–100 mV·s^{-1}) were collected and used to extract the double-layer capacitance. The EIS measurements for HER were performed at a 100-mV overpotential under the influence of an alternating current (ac) voltage of 50 mV from 100 kHz to 0.1 Hz. In addition, accelerated durability tests (ADT) were carried out at the voltage range of 0 V to −0.25 V (*versus* RHE) for 10^4 cyclic voltammetry cycles with a scan rate of 100 mV·s^{-1} in 1.0 M KOH. Chronopotentiometric tests at the continuous current density of 10 mA·cm^{-2} for HER were conducted to explore the stability of the electrocatalysts.

2.4. Computational methods

The density functional theory calculations presented in this paper were conducted using the Vienna *ab-initio* simulation package (VASP) software, developed at the University of Vienna. VASP employs the Perdew–Burke–Ernzerhof (PBE-GGA) scheme to calculate correlation potentials through the use of PBE functionals within the generalized gradient approximation (GGA). All calculations were performed using a plane-wave truncation energy of 600 eV, K-spaces was sampled using a $6 \times 6 \times 6$ grid, the energy convergence criterion was set to 10^{-5} eV, and the force was converged to less than 0.05 eV/Å for each ion, without consideration of van der Waals forces.

3. Results and discussion

3.1. Theoretical prediction

To investigate the influence of A-sites element on the intrinsic activity of $A\mathrm{Cu_3Ru_4O_{12}}$ (A = Na, Ca, Sr, Nd, and La), we firstly perform DFT calculations to identify the possible chemical configuration and evaluate the projected density of states (PDOS). Five atomic configurations [Fig. 1(a)] with analogous crystal structures are optimized and validated with reference to prior experimental and theoretical investigations.[34,35] The total PDOS of all quadruple perovskite oxides exhibits a crossing of the Fermi level, indicative of a typical metallic behavior [Fig. 1(b)].

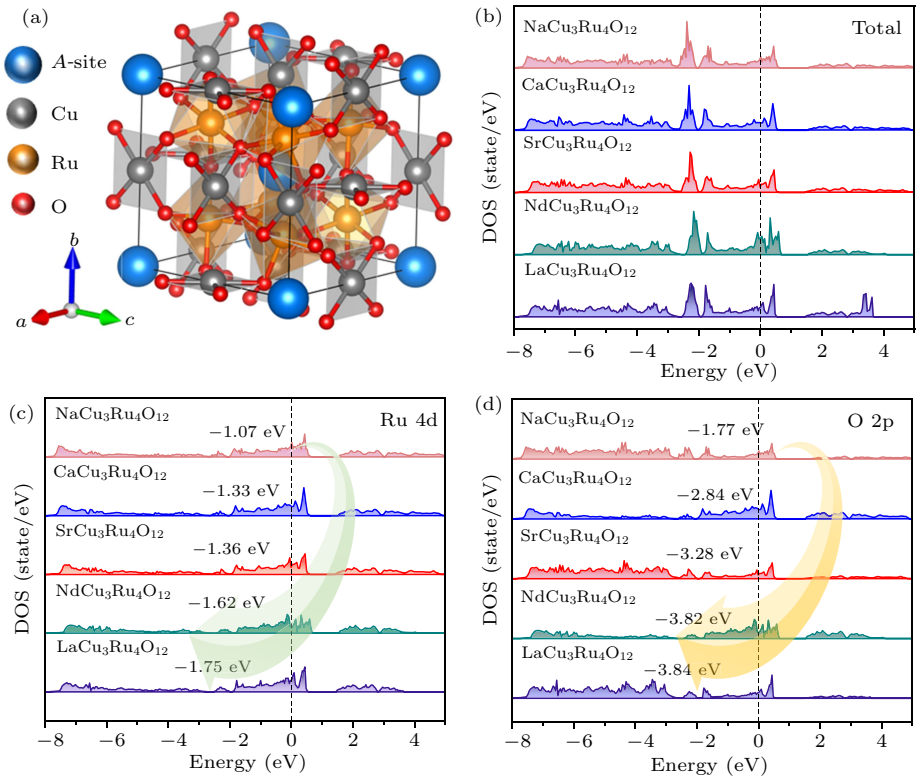


Fig. 1. (a) The model of DFT calculation of $A\mathrm{Cu_3Ru_4O_{12}}$ (A = Na, Ca, Sr, Nd, and La), (b) the total DOS, (c) the PDOS of Ru 4d. (d) The PDOS of O 2p.

This behavior contributes to the intrinsic catalytic activity of these materials, which is a consequence of their high electrical conductivity.[36] The d-band center and p-band center of electrocatalysts are closely related to the electrocatalytic activity, which can present the hybridization level.[37]

As shown in Fig. 1(c), the DOS of Ru 4d-band shifts toward the Fermi level from $LaCu_3Ru_4O_{12}$, $NdCu_3Ru_4O_{12}$, $SrCu_3Ru_4O_{12}$, $CaCu_3Ru_4O_{12}$, and $NaCu_3Ru_4O_{12}$, indiacating the increase of adsorption strength for Ru. Also, the trend of O p-band center exhibits a similar phenomenon, which gradually increases toward the Fermi level in the sequence of the above samples in Fig. 1(d). Similarly, the PDOS of Cu [see Fig. S1 in supporting information] contributes to the metallic properties, and a reasonable charge accumulation at the Fermi level would provide a linear control relationship for the catalytic process. The Ru 4d, Cu 3d, and O 2p orbitals devote the main electrons to realize suitable 4d–3d–2p orbital hybridization, which may optimize the binding energies of water and hydroxyl groups intermediates during HER. In conclusion, the theoretical calculations demonstrate that it is a viable strategy to enhance the HER activity of ruthenium-based quadruple perovskite though incorporating *A*-site elements. Moreover, a comprehensive understanding of the relationship between electronic configurations and their key effects on intermediates will be beneficial for establishing a robust descriptor platform.

3.2. Structural characterization

The process delineating the preparation of a series of $ACu_3Ru_4O_{12}$ (A = Na, Ca, Sr, Nd, and La) materials has been depicted in supporting information. Initially, x-ray diffraction (XRD) was utilized to confirm the phase structure. All samples crystallize into *A*-site-ordered quadruple perovskite-type structures, mainly belong to the cubic space group *Im*-3 (No. 204) in Fig. 2(a). Notwithstanding the inevitable presence of minute quantities of impurity phases (RuO_2, $SrRuO_3$, $CaRuO_3$), the principal phase of the sample can still be deemed to be essentially pure. All impurity phase ratios for $ACu_3Ru_4O_{12}$ are less than 5% by XRD refinement results (seeing below). The crystal structure can be conceptualized as a $2 \times 2 \times 2$ superlattice of ABO_3 (simple cubic perovskite). In the target sample $SrCu_3Ru_4O_{12}$, the distribution of Sr and Cu is orderly and exhibits a 1:3 ratio at the *A* site. Furthermore, the RuO_6 octahedra arrange regularly along with the distribution of corner-sharing at *B*-sites. Rietveld refinement of the XRD pattern reveals that $SrCu_3Ru_4O_{12}$ possesses a main cubic phase with a little impurity cubic phase for $SrRuO_3$ in Fig. 2(b). On the base of Rietveld refinements on diffraction data, the lattice parameter a and Ru–O bond length are determined to be 7.44878(3) Å and 1.9796(9) Å, which agrees with the reported values. Interestingly, the Ru–O bond lengths are regularly aligned in all samples [Fig. 2(c)], exhibiting a pattern that aligns with the distribution of the values of the Ru 4d-band and O 2p-band centers in the electronic density of states analysis. The crystal structure parameters and fitting results obtained for all samples based on XRD refinement can be seen in the Fig. S2 and Table S1, which is consistent with the calculated results (Table S2).

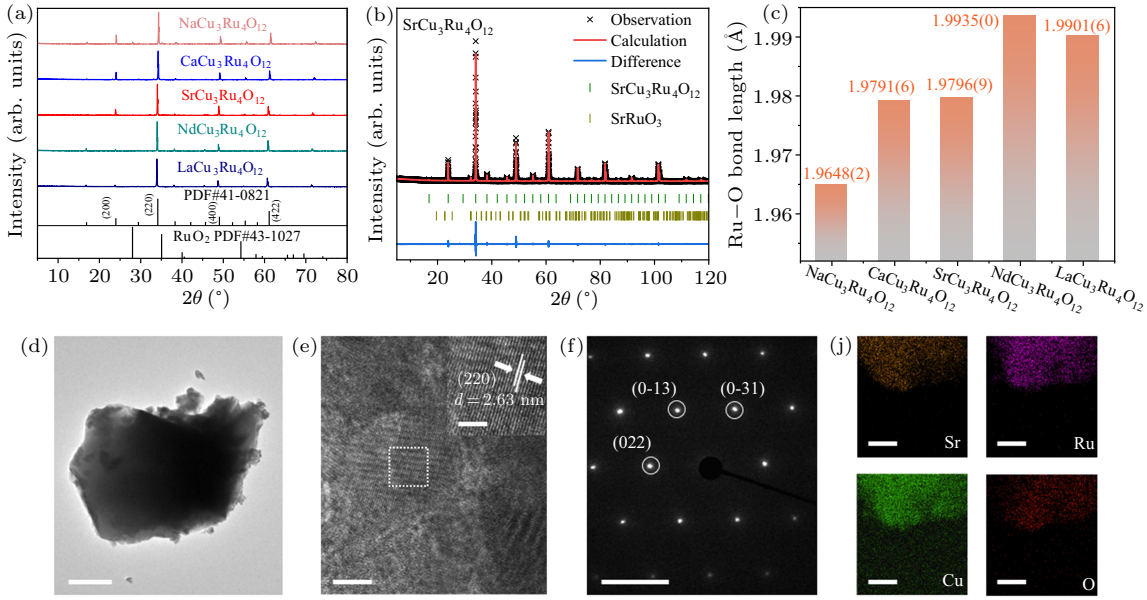


Fig. 2. (a) The XRD patterns of $ACu_3Ru_4O_{12}$ (A = Na, Ca, Sr, Nd, and La), (b) XRD pattern collected at room temperature and the corresponding Rietveld refinement results for $SrCu_3Ru_4O_{12}$, (c) the Ru–O bond length of $ACu_3Ru_4O_{12}$ (A = Na, Ca, Sr, Nd, and La) through refinement results, (d) TEM image of $SrCu_3Ru_4O_{12}$ (scale bar: 500 nm), (e) HR-TEM image of $SrCu_3Ru_4O_{12}$ (scale bar: 5 nm, and scale bar in inset image: 2 nm), (f) SAED image of $SrCu_3Ru_4O_{12}$ (scale bar: 5 nm^{-1}), (g) elemental distribution maps of $SrCu_3Ru_4O_{12}$ (scale bar: 250 nm).

The $SrCu_3Ru_4O_{12}$ exhibits a block structure at average size of 1 μm–10 μm as a typical perovskite morphology. High-resolution transmission electron microscopy (HR-TEM) image reveals fringes with a spacing of 2.63 Å, which corresponds to the (220) plane. The good crystallinity and phase structure are further confirmed by selected area elec-

tron diffraction (SAED) pattern in Fig. 2(e), align well with the XRD data. The elemental mapping at low and high magnification demonstrates that the spatial distribution of elements including Sr, Cu, Ru, and O, is consistent with the expected molar ratio. Other quadruple perovskite materials has been found to exhibit similar characterization, thereby confirming the results of previous studies indicating their synthetic homogeneity and morphological consistency [Fig. S3]. In conclusion, $ACu_3Ru_4O_{12}$ family represents an ideal research platform that offers the possibility of modulation of HER catalytic properties.

3.3. Electrochemical performance

Inspired by the distinctive crystal and electronic configuration properties of $ACu_3Ru_4O_{12}$ family, we evaluated its HER electrocatalytic performance. To facilitate comparison, we test the $ACu_3Ru_4O_{12}$ (A = Na, Ca, Sr, Nd, and La) oxides, which possess similar crystal structures in an alkaline medium using a three-electrode configuration in an Ar-saturated 1-M KOH solution. All sample electrochemical properties and parameters are seen in Table S3. The linear sweep voltammetry (LSV) polarization curves for various perovskite electrocatalysts on carbon paper are depicted in Fig. 3(a).

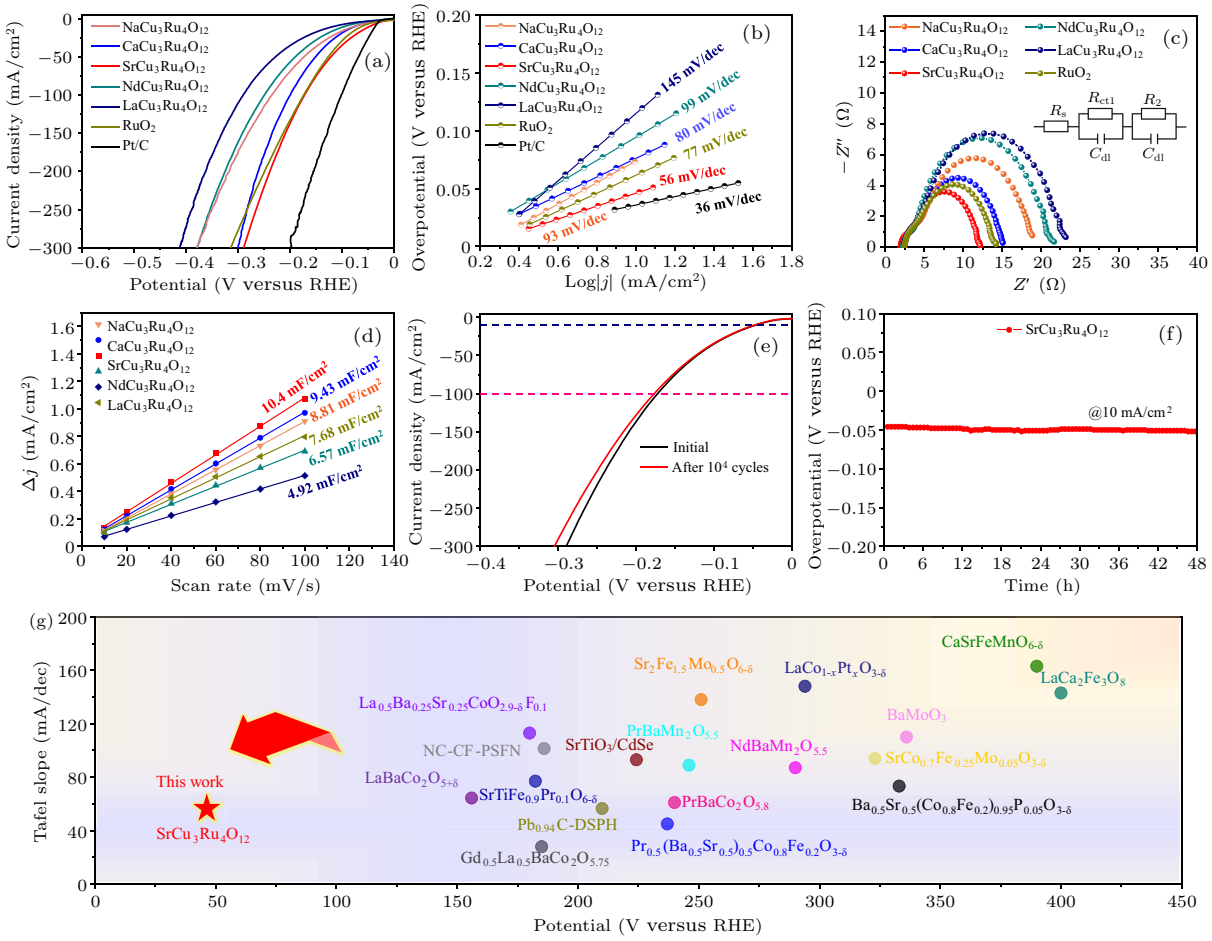


Fig. 3. Electrochemical HER properties of the catalysts: (a) LSV curves, (b) corresponding Tafel slopes, (c) Nyquist plots of EIS, (d) C_{dl} extracted from the CV plots, (e) ADT test, (f) chronopotentiometry (VT) of $SrCu_3Ru_4O_{12}$ at 10 mA·cm^{-2}, (g) overpotentials at the current density of 10 mA·cm^{-2} and the Tafel plots of $SrCu_3Ru_4O_{12}$ and other recently reported high performance HER catalysts.

Despite incorporating carbon powder into the $ACu_3Ru_4O_{12}$ family and loading it onto carbon paper to enhance electron transfer and distribute the quadruple perovskite oxides, the carbon materials demonstrate negligible HER activity. The overpotentials required for $NaCu_3Ru_4O_{12}$, $CaCu_3Ru_4O_{12}$, $SrCu_3Ru_4O_{12}$, $NdCu_3Ru_4O_{12}$, and $LaCu_3Ru_4O_{12}$ to achieve a current density of 10 mA·cm^{-2} are 46 mV, 74 mV, 75 mV, 94 mV, and 114 mV, respectively. It is noteworthy that $SrCu_3Ru_4O_{12}$ performs comparably to commercial Pt/C benchmarks at low current densities ($<$ 10 mA·cm^{-2}), but underperforms relative to Pt/C at higher current densities due to inadequate proton transfer capability. The Tafel slopes are measured to investigate the catalytic activity of these catalysts in alkaline HER. With a Tafel slope of 56 mV·dec^{-1}, the champion $SrCu_3Ru_4O_{12}$ exhibits the lowest overpotential among the perovskites in Fig. 3(b). This enhanced activity is likely attributed to the synergistic effects between the A-site elements and the Ru active sites. Electrochemical impedance spectroscopy (EIS) was conducted to elucidate the effects of electrical conductivity and investigate the electrode kinetics during the HER process.[38] Nyquist plots were recorded at an overpotential of 100 mV, where a smaller compressed semicircle signifies lower charge transfer resistance during HER. The resistance

(R_s), charge transfer resistance (R_{ct}), and low-frequency resistance (R_2) are detailed in the inset figure. The EIS data confirm that the $SrCu_3Ru_4O_{12}$ quadruple perovskite electrocatalyst exhibits exceptional charge transport performance and reduced resistance, demonstrating superior catalytic activity in the HER process, consistent with the LSV results in Fig. 3(c). To determine the number of active sites on the catalyst, the HER current density derived from electrochemical double-layer capacitance measurements was used [Fig. S4], with the current density normalized to the electrochemically active surface area (ECSA).[39] The advantages of the synergistic *A*-site and Ru sites are further evidenced by the larger double-layer capacitances (C_{dl}) at 10.4 mF/cm^2 observed in $SrCu_3Ru_4O_{12}$ in Fig. 3(d).

Beyond the activity previously discussed, the stability of the electrocatalyst is a pivotal factor in assessing its practical value. After 10^4 CV cycles, the optimal $SrCu_3Ru_4O_{12}$ catalyst exhibits only slight degradation in HER performance in Fig. 3(e). For further comparison, additional testing of the remaining chalcogenide samples is shown in Fig. S5 and Table S4. Moreover, in the durability evaluation via chronopotentiometry (VT) test, $SrCu_3Ru_4O_{12}$ maintained stable operation for over 48 hours at a current density of 10 mA·cm^{-2} in 1 M KOH in Fig. 3(f). Interestingly, the crystal structure of the $SrCu_3Ru_4O_{12}$ electrocatalyst remains well-preserved, as evidenced by the XRD patterns in Fig. S6. Additionally, the HR-TEM image obtained after the VT test shows high crystallinity similar to that observed before the reaction in Fig. S7, confirming the stability of the crystal structure. Moreover, a quantitative comparison with the literature indicates that the $SrCu_3Ru_4O_{12}$ electrocatalyst exhibits notably smaller overpotentials and Tafel slopes compared to the perovskite materials in Fig. 3(g) and Table S5.

3.4. Electron configuration and valence states analysis

During catalytic process, the surface layer of the sample furnishes a wealth of active sites that enhance the adsorption of reaction intermediates. To elucidate the surface catalytic mechanism related to charge configuration and valence transfer, x-ray photoelectron spectroscopy (XPS) was employed in Fig. 4. The survey spectrum of $ACu_3Ru_4O_{12}$ family predominantly features peaks corresponding to Na 1s, Ca 2p, Sr 3d, Nd 3d, La 3d, Cu 2p, Ru 3d, and O 1s, indicating the presence of these elements in the synthesized samples, as depicted in Fig. 4(a).

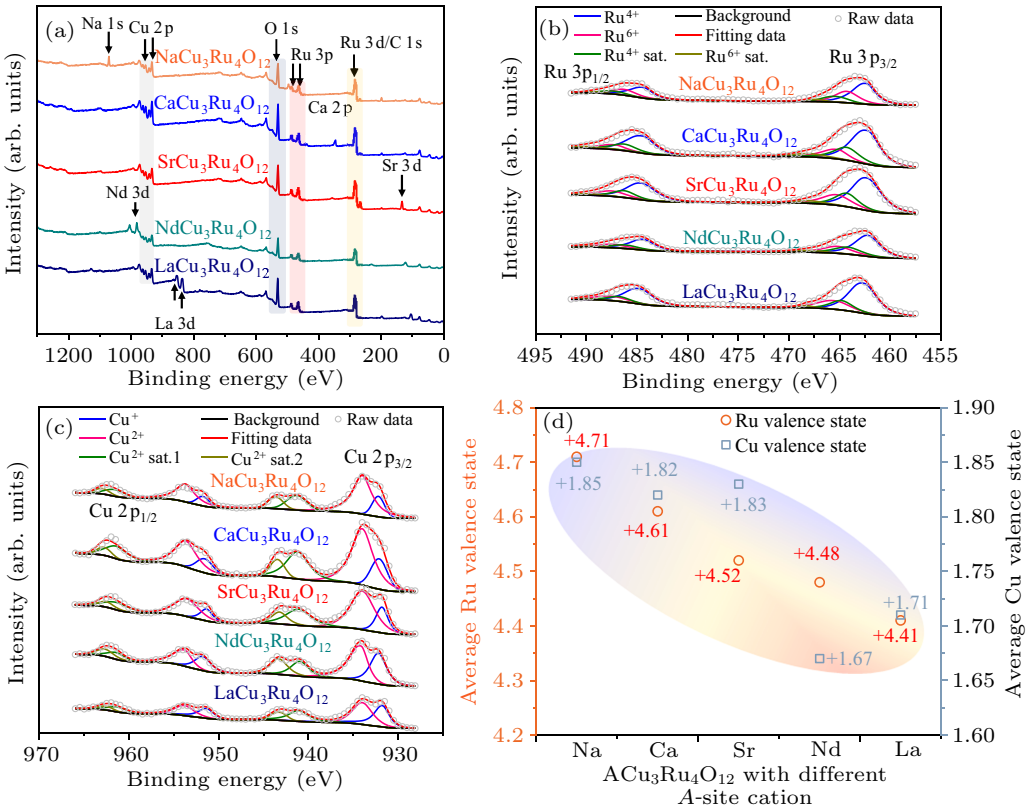


Fig. 4. The XPS spectrum of $A'Cu_3Ru_4O_{12}$ (A = Na, Ca, Sr, Nd, and La): (a) survey spectrum, (b) the Ru 3p, (c) the Cu 2p, (d) the average valence state of Ru and Cu.

Figure 4(b) illustrates the XPS spectra for the Ru 3p region of $ACu_3Ru_4O_{12}$ (A = Na, Ca, Sr, Nd, and La). The original spectra were deconvoluted into multiple peaks using Gauss–Lorentz functions. The fitted peak positions at approximately 462.3 eV and 464.3 eV correspond to Ru^{4+} and Ru^{6+}, respectively,[32] with two satellite peaks: Ru^{4+} sat. and Ru^{6+} sat., observed at approximately 465.3 eV and 468 eV. The estimated average valence states of the Ru element in $A'Cu_3Ru_4O_{12}$ (A = Na, Ca, Sr, Nd, and La) are +4.72, +4.61, +4.52, +4.48, and +4.41, respectively. Figure 4(c) presents

the XPS core-level spectra of Cu 3d, which have been deconvoluted into four peaks centered at ∼ 931.8 eV (Cu^{2+}), ∼ 934.0 eV (Cu^{+}), ∼ 941.1 eV (Cu^{2+} sat.1), and ∼ 943.2 eV (Cu^{2+} sat.2), respectively.[40,41] By comparing the fitted areas, the average valence of Cu in $A'Cu_3Ru_4O_{12}$ (A = Na, Ca, Sr, Nd, and La) is +1.84, +1.83, +1.82, +1.71, and +1.67, respectively. Given that Na is typically monovalent, Ca and Sr are generally divalent, and Nd and La are commonly trivalent, it is notable that the average valence distributions of Ru and Cu exhibit a negative linear relationship with the valence distribution of the A-site ion, as shown in Fig. 4(d). Charge transport within the Ru–O octahedra is facilitated by the overlapping electron cloud interactions at the A-site and oxygen site. This reflects a charge transfer and a shift in the valence of the Cu and Ru elements across the oxygen bridge, driven by changes in the electronegativity of the A-site ions.

3.5. HER enhancement mechanism and electronic configuration descriptor

In the subsequent phase, we examine the band center of Ru 4d and O 2p, the value of Ru and Cu and the Ru–O bond length to elucidate their relationship with the hydrogen evolution reaction (HER) activity and stability within our quadruple perovskite series $A'Cu_3Ru_4O_{12}$ (A = Na, Ca, Sr, Nd, and La). The overpotential at 100 mA·cm^{-2} for each sample provides a measure of intrinsic catalytic activity, while the potential decay following 10^4-CV cycles serves as an indicator of catalytic stability. Given that the tunability of the d-band center is considered a fundamental property that can modulate the hydrogen evolution reaction (HER) intermediate H* adsorption capacity, it is recognized as a valid descriptor. Wang *et al.* manipulated the d-band center position and established a linear relationship between the d-band center and ΔG_{H^*}, elucidating the adsorption sites for H* on Ni–M alloys.[42] We find the band center between Ru 4d and O 2p can be rationally with correlated with the intrinsic HER activity and the valence state factor of Ru and Cu can be similarly applicable to guide the quadruple perovskite activity in Figs. 5(a) and 5(b).

Additionally, the Ru–O band length, which can roughly represent the Ru–O bond energy, with overpotential shows an approximate volcano diagram shape in Fig. 5(c). This suggests

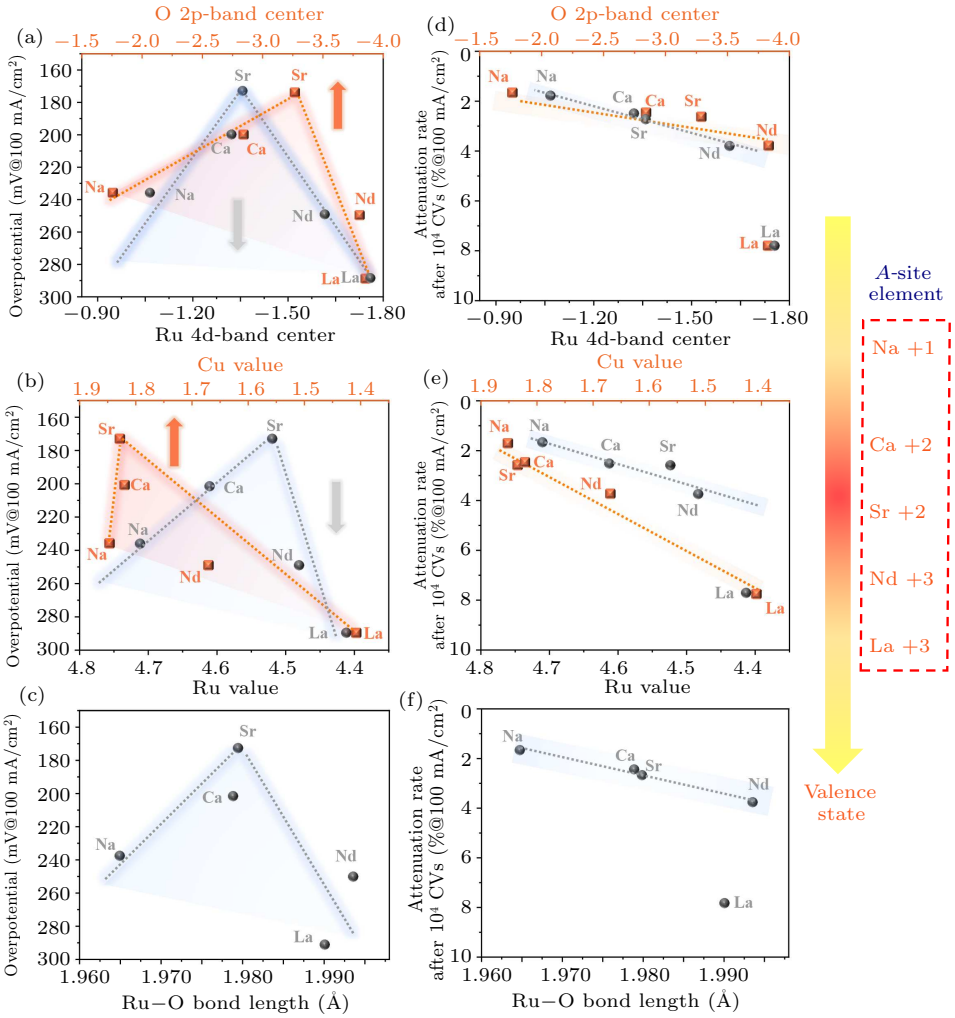


Fig. 5. Correlation with intrinsic HER activity and stability. HER activity trends of overpotential at 100 mA·cm^{-2} as a function of (a) Ru 4d-band center and O 2p-band center, (b) the valence state of Ru and Cu, and (c) the Ru–O bond length for quadruple perovskite family. Attenuation rate after 10^4 CVs at 100 mA·cm^{-2} as a function of (d) Ru 4d-band center and O 2p-band center, (e) the valence state of Ru and Cu, and (f) the Ru–O bond length for quadruple perovskite family.

that the electronegativity and valence differences of the *A*-site elements resulted in altering the Ru electronic structure within the system upon introduction. This modest 4d–3d–2p orbital hybridization among Ru, Cu, and O elements activates the electron transfer.[43] The optimization of electron density occupation state is also shown to be a significant contributor to the electron reflux between Ru and Cu. The optimized ruthenium sites exhibit moderate adsorption and dissociation of intermediates, which likely accounts for the strongest intrinsic catalytic activity.

In prior studies, the stability of catalytic materials has rarely been associated with descriptors due to complexities of diverse catalytic reactions and intricate mechanisms governing surface proton-electron transfer.[44] Interestingly, electrochemical stability gradually decreases as the band-center moves away from the Fermi level in Fig. 5(d). Similarly, a significant negative correlation is shown with Ru valence and Cu valence and stability in Fig. 5(e). This is also reflected in the relationship between the length of the Ru–O bond and the decay ratio in Fig. 5(f). This may be attributed to the charge accumulation and valence decrease of the active site Ru, which could render it more susceptible to reduction effects and surface remodeling under reducing potentials. Such changes might disrupt the crystal structure and compromise catalytic performance.[45] The construction of volcano diagrams and the establishment of inverse linear relationships regarding the quadruple perovskite family provide a framework, for understanding how Ru-based systems can optimize orbital hybridization and electronic structure modulation to enhance activity and stability. It also provides valuable datasets of catalytic parameters for investigating descriptors using large models such as machine learning (ML) and artificial intelligence (AI).

Following the above guidance program, we propose possible HER mechanism. When we assume that the local crystal structures of target sample $SrCu_3Ru_4O_{12}$ are reacted on the surface at a certain level, the possible HER routes are shown in Fig. 6. Through judge the Tafel slope in $SrCu_3Ru_4O_{12}$ (56 mV/dec), we believe that the rate-determining step (RDS) of HER can be evaluated as Volmer–Heyrovsky path. Subsequent to the Volmer step for water dissociation, the OH^- ions that are generated must undergo desorption from the catalyst surface to facilitate the regeneration of the active sites in Figs. 6(I)–6(III).[46–48] Simultaneously, the H^* species are simultaneously adsorbed onto the active sites, where they are subsequently recombined with H_2 in Fig. 6(IV). Ru-based quatrle perovskite offer localized proton reservoir to enhance actibity to dissociative complexation with water nolecules. Moreover, the unique structure including frakework between square-planar CuO_4 and heavy tilting RuO_6 octahedra make sure the stable platform to HER process.

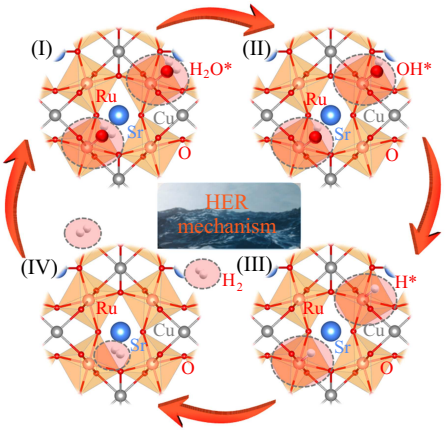


Fig. 6. The HER catalytic mechanism schematic diagram. The orange octahedra represent RuO_6. The red area represents the reaction sites.

4. Conclusion

In conclusion, we developed the quadruple perovskite iridate oxide $SrCu_3Ru_4O_{12}$ as a superior OER catalyst with high activity and excellent stability for alkaline water oxidation. At density of 10 $mA{\cdot}cm^{-2}$, the catalyst presented a ultralow overpotential of 46 mV and a low Tafel slope of 56 mV/dec. In addition, much better durability, up to 10^4 CVs and 48 h, was also exhibited by this Ru-based compound. We showcase the descriptor of Ru location electron environment via d-band center, valence state, and Ru–O bond length, to efficiently screen high-performance perovskites synthesized for alkaline HER. Combined XPS and DFT studies demonstrate that the with the change in electronegativity of the *A*-site element, 4d–3d–2p orbital hybridization has taken place and induced super-exchange interaction to the exchange of electrons between the Ru and Cu elements via an oxygen bridge. A moderate Ru-site electronic configuration would facilitate the adsorption and subsequent dissociation of the intermediate; while suilable framework of between square-planar CuO_4 and tilting RuO_6 octahedra maintains the crystal structure to enhance the stability during HER. This work not only demonstrates a new family $ACu_3Ru_4O_{12}$ oxide as an efficient HER catalysts, but also proposes a proper modulation strategy from the perspective of precise descriptor to predict high effient catalyst.

Acknowledgements

Project supported financially by the National Key Research and Development Program of China (Grant No. 2023YFA1406000), the National Natural Science Foundation of China (Grant Nos. 22171283 and 12474002), the Fundamental Research Funds for the Central Universities (Grant Nos. 2023ZCJH03 and 2021XD-A041), the Fund of State Key Laboratory of Information Photonics and Optical Communications (Beijing University of Posts and Telecommunications, China), the Teaching Reform Projects at BUPT (Grant No. 2022CXCYB03), and the BUPT Excellent Ph.D. Students Foundation (Grant No. CX2023108). We would like to thank

Shiyanjia Laboratory (www.shiyanjia.com) for the support of XPS test.

References

[1] Mahmood N, Yao Y, Zhang J W, Pan L, Zhang X W and Zou J J 2018 *Adv. Sci.* **5** 1700464

[2] Guan D Q, Wang B W, Zhang J G, Shi R, Jiao K, Li L, Wang Y, Xie B, Zhang Q W, Yu J, Zhu Y F, Shao Z P and Ni M 2023 *Energy Environ. Sci.* **16** 4926

[3] Bergero C, Gosnell G, Gielen D, Kang S, Bazilian M and Davis S J 2023 *Nat. Sustain* **6** 404

[4] Chen Z G, Gong W B, Wang J, Hou S, Yang G, Zhu C F, Fan X Y, Li Y F, Gao R and Cui Y 2023 *Nat. Commun.* **14** 5363

[5] Deng C, Toe C Y, Li X, Tan J J, Yang H P, Hu Q and He C X 2022 *Adv. Energy Mater.* **12** 2201047

[6] Jiang Y, Fu H, Liang Z, Zhang Q and Du Y P 2023 *Chem. Soc. Rev.* **53** 714

[7] Singh K, Tetteh E B, Lee H Y, Kang T H and Yu J S 2019 *ACS Catal.* **9** 8622

[8] Zhang S, Li J and Wang E 2020 *ChemElectroChem* **7** 4526

[9] Yang Y J, Yu Y H, Li J, Chen Q R, Du Y L, Rao P, Li R S, Jia C M, Kang Z Y, Deng P L and Shen Y J 2021 *Nano-Micro Lett.* **13** 160

[10] Li H J W, Liu K, Fu J W, Chen K J, Yang K X, Lin Y Y, Yang B P, Wang Q Y, Pan H, Cai Z J, Li H M, Cao M Q, Hu J H, Lu Y R, Chan T S, Cortés E, Fratalocchi A and Liu M 2021 *Nano Energy* **82** 105767

[11] Zhang Z, Li P, Wang Q, Feng Q, Tao Y K, Xu J Y, Jiang C, Lu X E, Fan J T, Gu M, Li H and Wang H J 2019 *J. Mater. Chem. A* **7** 2780

[12] Liu W Q, Chen Q W, Shang Y X, Liu F, He R L, Zhang J Y, Li Q L, Chai H, Tan Y Y and Bao S J 2024 *Adv. Funct. Mater.* 2410325

[13] Luo J Q, Sun Y Q, Liu P L, Zhong S M, Li Y G, Zhang R L, Zhang P, Chi Y L, Xu H, Wei Y C, Song W Y, Li Z X and Liu J 2024 *ACS Sustainable Chem. Eng.* **12** 5319

[14] Wu Z H, Liu L C, Zhao Z Y, Yang C D, Mu S D, Zhou H J, Luo X L, Ma T, Li S and Zhao C S 2023 *Small* **19** 2204738

[15] Zhao J, Urrego-Ortiz R, Liao N, Calle-Vallejo F and Luo J S 2024 *Nat. Commun.* **15** 6391

[16] Lu Q, Zou X H, Bu Y F, Wang Y and Shao Z P 2024 *Energy Storage Mater.* **68** 103341

[17] Huang Z N, Li T T, Li B Y, Dong Q, Smith J, Li S, Xu L, Wang G F, Chi M F and Hu L B 2024 *J. Am. Chem. Soc.* **146** 2167

[18] Ye X B, Song S Z, Li L L, Chang Y C, Qin S J, Liu Z H, Huang Y C, Zhou J, Zhang L J, Dong C L, Pao C W, Lin H J, Chen C T, Hu Z W, Wang J Q and Long Y W 2021 *Chem. Mater.* **33** 9295

[19] Yu R Z 2024 *Chin. J. High Press. Phys.* **38** 010102

[20] Wang X, Liu Z H, Lu D B, Pi M C, Pan Z and Long Y W 2024 *Chin. J. High Press. Phys.* **38** 010101

[21] Lv Y X, Li F Y and Jin C Q 2012 *Chin. J. High Press. Phys.* **23** 31

[22] Zhu Y L, Tahini H A, Hu Z W, Dai J, Chen Y B, Sun H N, Zhou W, Liu M L, Smith S C, Wang H T and Shao Z P 2019 *Nat. Commun.* **10** 149

[23] Dai J, Zhu Y L, Tahini H A, Lin Q, Chen Y, Guan D Q, Zhou C, Hu Z W, Lin H J, Chan T S, Chen C T, Smith S C, Wang H T, Zhou W and Shao Z P 2020 *Nat. Commun.* **11** 5657

[24] Yagi S, Yamada I, Tsukasaki H, Seno A, Murakami M, Fujii H, Chen H R, Umezawa N, Abe H, Nishiyama N and Mori S 2015 *Nat. Commun.* **6** 8249

[25] Yamada I, Takamatsu A, Asai K, Ohzuku H, Shirakawa T, Uchimura T, Kawaguchi S, Tsukasaki H, Mori S, Wada K, Ikeno H and Yagi S 2018 *ACS Appl. Energy Mater.* **1** 3711

[26] Miao X, Zhang L, Wu L, Hu Z P, Shi L and Zhou S M 2019 *Nat. Commun.* **10** 3809

[27] Ding J and Zhu X H 2024 *J. Mater Chem. C* **12** 9510

[28] Calle-Vallejo F 2023 *Adv. Sci.* **10** 2207644

[29] Liu J W, Luo W Z, Wang L, Zhang J J, Fu X Z and Luo J L 2022 *Adv. Funct. Mater.* **32** 2110748

[30] Wang B and Zhang F X 2022 *Angew. Chem. Int. Ed.* **61** e202111026

[31] Liu J Y, Liu H, Chen H J, Du X W, Zhang B, Hong Z L, Sun S H and Wang W C 2020 *Adv. Sci.* **7** 1901614

[32] Pang S L, Xu J, Su Y J, Yang G M, Zhu M, Cui M, Shen X Q and Chen C L 2020 *Appl. Catal. B-Environ.* **270** 118868

[33] Guan D, Zhou J, Huang Y C, Dong C L, Wang J Q, Zhou W and Shao Z P 2019 *Nat. Commun.* **10** 3755

[34] Kobayashi W, Terasaki I, Takeya J I, Tsukada I and Ando Y 2004 *J. Phys. Soc. Jpn.***73** 2373

[35] Tang L L, Shi S P, Song Y, Hu J B, Diao K, Jiang J, Duan Z J and Chen D L 2023 *Chin. Phys. B* **32** 066106

[36] Bielański A, Dereń J and Haber J 1957 *Nature* **179** 668

[37] Liu Y D, Sakthivel T, Hu F, Tian Y H, Wu D S, Ang E H, Liu H, Guo S W, Peng S J and Dai Z F 2023 *Adv. Energy Mater.* **13** 2203797

[38] Wang Y X, Yang Q, Liu C, Wang G X, Wu M, Liu H, Sui Y M and Yang X Y 2020 *Chin. Phys. Lett.* **37** 058201

[39] Huang K, Lin C L, Yu G Q, Du P, Xie X Y, He X, Zheng Z C, Sun N, Tang H L, Li X B, Lei M and Wu H 2023 *Adv. Funct. Mater.* **33** 2211102

[40] Liu W, Kawano K, Kamiko M, Kato Y, Okazaki Y, Yamada I and Yagi S 2022 *Small* **18** 2202439

[41] Jones S D, Neal L M, Everett M L, Hoflund G B and Hagelin-Weaver H E 2010 *Appl. Surf. Sci.* **256** 7345

[42] Wang J S, Xin S S, Xiao Y, Zhang Z F, Li Z M, Zhang W, Li C J, Bao R, Peng J, Yi J H and Chou S L 2022 *Angew. Chem.* **134** e202202518

[43] Sun N, Zheng Z C, Lai Z Z, Wang J J, Du P, Ying T P, Wang H F, Xu J C, Yu R Z, Hu Z W, Pao C W, Huang W H, Bi K, Lei M and Huang K 2024 *Adv. Mater.* **36** 2404772

[44] Exner K S 2019 *ChemCatChem* **11** 3234

[45] Sun N, Lai Z Z, Ding W B, Li W B, Wang T Y, Zheng Z C, Zhang B W, Dong X J, Wei P, Du P, Hu Z W, Pao C W, Huang W H, Wang H F, Lei M, Huang K and Yu R Z 2024 *Adv. Sci.* 2406453

[46] Fu G S, Gao H Z, Yang G W, Yu P and Liu P 2022 *Chin. Phys. B* **31** 077901

[47] Lin G X, Zhang Z, Ju Q J, Wu T, Segre C U, Chen W, Peng H R, Zhang H, Liu Q N, Liu Z, Zhang Y F, Kong S Y, Mao Y L, Zhao W, Suenaga K, Huang F Q and Wang J C 2023 *Nat. Commun.* **14** 280

[48] Ahmad A, Nairan A, Feng Z, Zheng R M, Bai Y L, Khan U and Gao J K 2024 *Small* **20** 2311929